
Article:
Chandrasekhar, K., Stevanovic, N., Cross, E. et al. (2021) Damage detection in operational wind turbine blades using a new approach based on machine learning. Renewable Energy, 168. pp. 1249-1264. ISSN: 0960-1481

https://doi.org/10.1016/j.renene.2020.12.119

Damage detection in operational wind turbine blades using a new approach based on machine learning

Kartik Chandrasekhar[a,*], Nevena Stevanovic[b], Elizabeth J. Cross[a], Nikolaos Dervilis[a], Keith Worden[a]

[a] *Dynamics Research Group, Department of Mechanical Engineering, University of Sheffield, Mappin Street, Sheffield, S1 3JD, UK.*
[b] *Siemens Gamesa Renewable Energy A/S, Borupvej 16, 7330 Brande, Denmark*

Abstract

The application of reliable structural health monitoring (SHM) technologies to operational wind turbine blades is a challenging task, due to the uncertain nature of the environments they operate in. In this paper, a novel SHM methodology, which uses Gaussian Processes (GPs) is proposed. The methodology takes advantage of the fact that the blades on a turbine are nominally identical in structural properties and encounter the same environmental and operational variables (EOVs). The properties of interest are the first edgewise frequencies of the blades. The GPs are used to predict the edge frequencies of one blade given that of another, after these relationships between the pairs of blades have been learned when the blades are in a healthy state. In using this approach, the proposed SHM methodology is able to identify when the blades start behaving differently from one another over time. To validate the concept, the proposed SHM system is applied to real onshore wind turbine blade data, where some form of damage was known to have taken place. X-bar control chart analysis of the residual errors between the GP predictions and actual frequencies show that the system successfully identified early onset of damage as early as six months before it was identified and remedied.

Keywords: structural health monitoring, wind turbine blades, machine

*Corresponding author
Email address: k.chandrasekhar@sheffield.ac.uk (Kartik Chandrasekhar)

learning, Gaussian processes, SCADA

1. Introduction

Wind turbines rely on a number of structurally-critical components that may directly affect their power generation capabilities. Of note are the tower, the gearbox and generator (for variable-speed wind turbines), the magnetic drive (for direct-drive wind turbines), various bearings (such as main bearings), and perhaps most importantly, the blades [1]. Blades are among the most expensive components - depending on their size; their manufacturing costs range between 10% and 20% of total manufacturing costs [2]. In recent years, blades have progressively become larger, to harvest more energy, and maximise power production. At the same time, since larger blades are associated with larger weight penalties, blade designs have continually been modified to keep the penalties low. These compromises have led to more flexible blades, and therefore, lower safety margins [3, 4].

Cracks and delaminations are reported to be the most common form of damage in blades [3]; these typically occur close to the blade root since this is the region where the blades experience the highest bending strains due to turbine rotation; this is especially true when taking large blades into consideration. Towards the end of the design lifetime of the blades, damage mechanisms become accentuated during excessive levels of winds, lightning strikes, and ice accumulation (which leads to rotor imbalance problems). It is extremely important to avoid critical blade failures, because when damaged blades liberate, they have the potential to damage not only the turbines they were attached to, but also other turbines in their vicinity [5].

There have also been heavy investments in the offshore wind industry, whereby wind turbines have increasingly been deployed on various seas and oceans, where wind conditions are favourable for energy production [6]. However, this freedom has come at a cost of ease of maintenance, since it is significantly more expensive to send technicians to inspect offshore structures via expensive transportation

[7].

For all these reasons, Structural Health Monitoring (SHM) technologies have become appealing to both wind turbine manufacturers and operators alike. The use of SHM technologies has largely been driven by a number of factors:

1. minimisation of downtime,
2. maximisation of reliability,
3. minimisation of operation and maintenance costs, and
4. extension of design lifetimes of monitored structures.

Currently, most of the focus in SHM research on small-to-medium sized blades has been in laboratory environments, where conditions are controlled. Additionally, researchers have had the luxury of multiple sensors and data acquisition systems with high sampling rates. Signals captured by these sensors include strains [8, 9], velocities [10], accelerations [11], acoustic emissions [8, 12, 13], guided waves [14, 15], thermographic images [16], and digital image correlation (DIC) images [17], to name a few. This type of monitoring has facilitated high-fidelity diagnostics (indication and location of damage), as well as prognostics (remaining life prediction). There have been numerous methods and procedures to aid in damage indication and localisation; these include changes in stiffness [18, 19] and modal properties [20], principal component analysis [9], image processing of thermographic [16] and DIC images [17], etc. Machine learning algorithms, such as artificial neural networks, have also been used previously [14].

The above-mentioned research subjects are extremely valuable, as they illustrate various routes to tackle the ultimate goal of having a reliable SHM system. However, operational wind turbines around the world face challenges that cannot be replicated in laboratory environments. Due to this issue - at least for the time being - certain methods can seem to be impractical. Some of the challenges are listed below.

- Firstly, there are significant costs involved in applying numerous sensors with high data-acquisition rates; these include the costs of the sensors

themselves, as well as costs associated with data storage and processing. One must also consider the fact that there are hundreds of thousands of wind turbines spread across the world.

- Furthermore, monitoring and diagnostic systems need to be designed to be robust to the heavily nonstationary conditions that wind turbines face. Nonstationarity primarily stems from constantly-changing wind and loading conditions (gusts, turbulence, etc.), and taking these into account is therefore a challenging task.

- Damage localisation is another challenge in operational wind turbines, since this is a function of excitation frequency and number of sensors, as well as data-acquisition rates and sensor placement. There are additional limitations as well; for example, one cannot place piezoelectric sensors along the length of the blades due to the risks associated with electromagnetic interference and lightning strikes.

- Diagnostic methods also need to find a balance between true and false positives, and this would involve a cost-benefit analysis. For example, in a laboratory, a 3% false positive rate may be deemed acceptable, but in the real world, if all turbines are stopped for 3% of the time, costs associated with downtime will have to be borne by turbine operators. On the other hand, if it does turn out that a damage indicator is correct, and the damage becomes irreparable, costs associated with blade replacement can also be considerable.

This article proposes methodologies that address some of these challenges. As mentioned above, when turbines are operating, the effects of environmental and operational variables cause significant nonstationarity; this is especially true of the frequency response of the blades. For example, high wind speeds can cause faster rotation of the turbines, which lead to stiffer blades and higher natural frequencies; higher temperatures lead to less stiff blades, hence lowering the natural frequencies. The methodologies proposed in this article take advantage

of the fact that the EOVs act simultaneously on all three blades. Therefore, when the monitored structural frequencies are viewed relative to each other, the complex nonstationarities are transformed into a simpler, and more explicable space. As a result of this transformation, it is possible to learn relationships between these monitored variables (as well as other EOVs). These relationships are learnt, in pairs, using probabilistic regression in the form of Gaussian Processes (GPs). The GPs are then used for predictive purposes, and the residuals between the actual signals and predicted signals can be used as an informative damage indicator.

The SHM scheme proposed is summarised in the next section. This is followed by a detailed review of the theory behind GPs. The article is complemented by three case studies of onshore wind turbines, where the proposed methodologies were applied, and would have successfully identified damage in advance of critical failure. It should be noted that the versatility of this methodology means that they can also be applied to offshore wind turbines.

2. Methodology

Figure 1 illustrates a summary of the SHM system that is presented in this article.

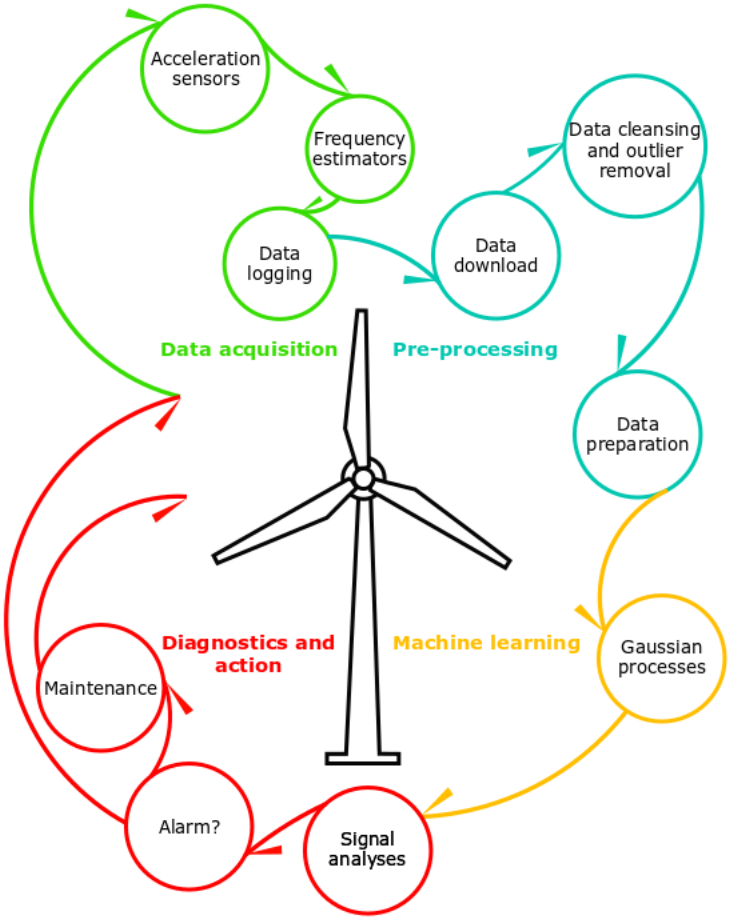

Figure 1: Summary of proposed SHM system

As shown in Figure 1, the SHM system capability is divided into four categories: data acquisition, pre-processing, machine learning, and diagnostics and actions; these are discussed in detail next.

2.1. Data acquisition

Acceleration sensors, and sensors that measure the environmental and operational variables (EOVs) measure the respective signals. The edge frequencies of each blade (i.e. the frequencies of the first bending mode in the blade edgewise direction) are estimated from the acceleration signals. In this paper, the

machine learning techniques are applied to Supervisory Control and Data Acquisition (SCADA) data. For readers unfamiliar with the SCADA system, it is a utility that acquires data from sensors mounted on a structure, and sends them to a central computer for monitoring and control purposes. The data statistics are logged at regular intervals, and these are typically ten-minute averages [21], which implies that the SCADA data has a low-pass filter applied to it. The variables used from the SCADA data include:

1. edge frequencies of each blade (in Hz),
2. ambient temperature (in °C),
3. power output (in W),
4. generator rotation speed (in RPM), and
5. pitch angle (in °).

Prior to data logging into the SCADA system, the individual signals are usually sampled at a rate of 10 Hz (in some cases, higher sampling is also possible). The aim of this work is to detect long term damage, which typically occurs over the course of several weeks or months. Therefore, although the data in the SCADA system have a low-pass filter applied to them, they are still capable of identifying the long term degradation in the blade stiffness, and hence the edge frequency. The benefit of using SCADA data over the higher-resolution data is that it saves processing time quite considerably.

2.2. Pre-processing

In this part of the system, SCADA data from the respective channels were downloaded from a number of wind turbines whose blades were known to have incurred damage. These time-series were then filtered, and processed to remove outliers within the data. Outliers are quite a common occurrence in SCADA data, and typically occur in the data logging process. Furthermore, since the time-series are logged in various dedicated channels, occasionally, it is common for data to not be recorded at certain times in a given channel, whilst data in other channels are being logged. It is possible to resample the data such that

all data channels have identical sampling rates. However, this requires some form of interpolation, which could result in misleading information. Therefore, it was decided that only data that had common timestamps would used for the remainder of the processing that followed.

Note that all the data used for the purposes of this article have been normalised prior to the application of the machine learning and signal processing methods. This is performed according to,

$$x_{norm} = \frac{x - \mu}{\sigma} \tag{1}$$

where the x are the data being normalised, μ is the mean, and σ is the standard deviation of selected training data. The selection of training data will be discussed shortly, but it is the same training data that will be used in the training of the Gaussian Processes (GPs). There are two primary reasons for normalising the data.

- To avoid numerical instabilities that may occur in various computations in GP inference.
- To avoid disclosing confidential information regarding blade properties.

Next, the various features were analysed to assess whether they contributed to the observed properties of the blade (i.e. the edge frequencies). Figure 2 shows a representative example of how the estimated edge frequencies of each blade correlate to each other. Note that the three blades on the turbine have been labelled A, B, and C.

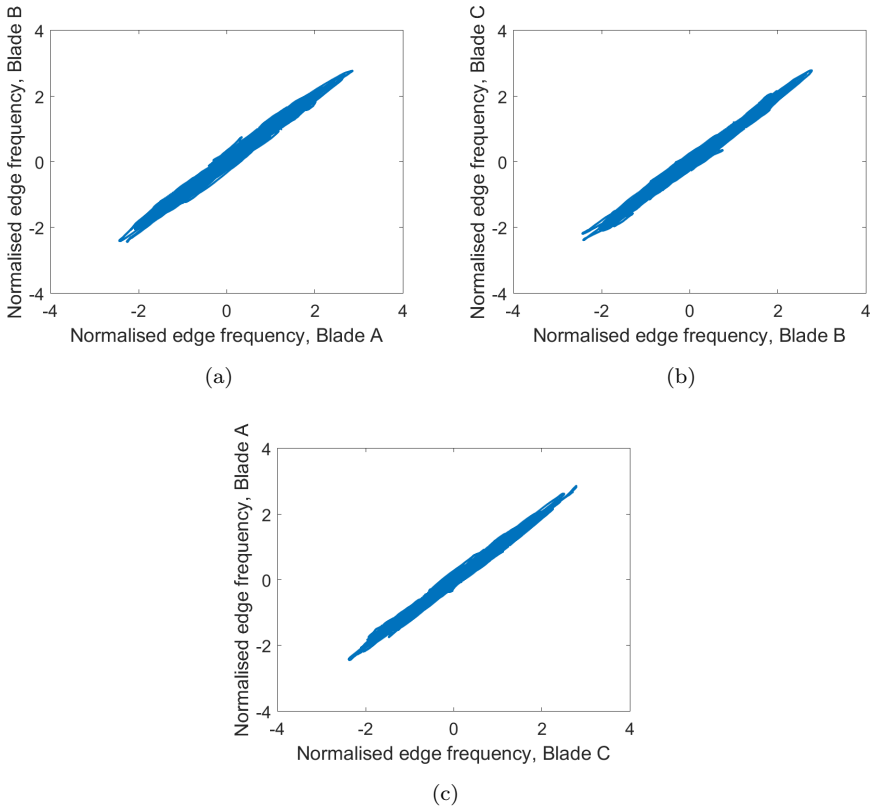

Figure 2: Correlation between normalised edge frequencies for: (a) Blade A vs. Blade B, (b) Blade B vs. Blade C, and (c) Blade C vs. Blade A.

Based on Figure 2, it is clear to see that these frequencies correlate well with each other in a linear fashion. Over time, as the blades age, the correlations generally worsen, and when damage occurs, the relationships generally break down. Therefore, the primary motivation behind the SHM system was to evaluate when the correlations worsened and/or broke down. It should be noted here that for the examples of correlations shown in Figure 2, simple methods such as Bayesian linear regression would be sufficient rather than the more complicated GPs. However, as shall be seen later, the correlations between the edge frequencies of each blade during normal condition are typically not as linear and noise-free on other wind turbines (see Figure 12). Since GPs are more robust

to such scenarios (since the functional forms need not be predetermined), they are the chosen method for this work.

175 Apart from the study of correlations between the respective edge frequencies, correlations between other EOVs and the edge frequencies of each blade were also studied. Figures 3 (a) to (d) illustrate exemplar relationships between the EOVs (ambient temperature, power output, generator rotation speed, and pitch angle, respectively) with respect to the estimated frequencies.

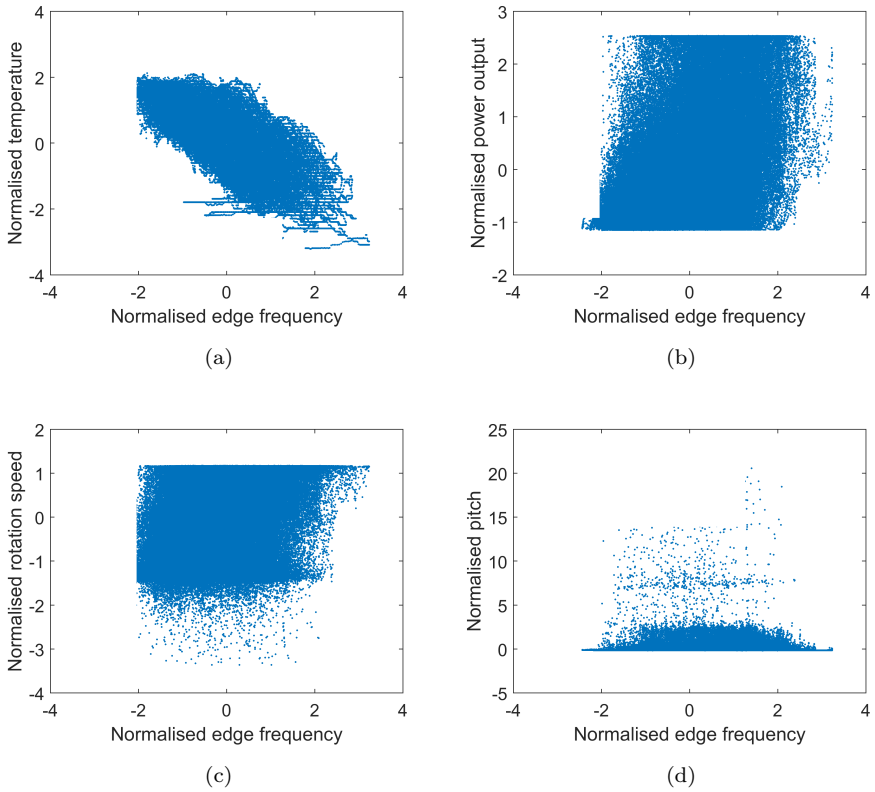

Figure 3: Correlation between normalised edge frequencies and normalised: (a) ambient temperature, (b) power output, (c) generator rotation speed, and (d) pitch angle.

180 As is indicated in Figure 3, it was found that, out of the EOVs considered, only the ambient temperature had any systematic influence on the estimated frequencies. When the estimated frequencies and temperatures are viewed over

time, it is evident that the cyclical nature of the estimated frequencies occur due to the seasonal variations, as shown in Figure 4.

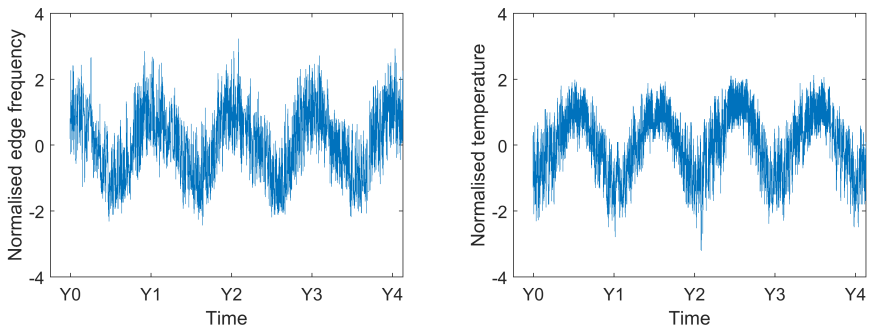

Figure 4: Time series of normalised: (a) frequency, and (b) ambient temperature.

The use of these EOVs (other than ambient temperature) in the machine learning tasks that follow were expected to lead to less accurate GP predictions since they do not contribute to the observed behaviour of the edge frequencies. Due to this fact, only the edge frequencies and ambient temperature features were selected for further processing.

In the next section, the theory of Gaussian processes (GPs) is provided.

2.3. Gaussian Processes

Gaussian processes (GPs) implement a nonparametric probabilistic regression. They are best understood in terms of a function space viewpoint [22]. Let $\boldsymbol{X}$ be an $N \times d$ matrix of inputs $\{\boldsymbol{x}_1, \boldsymbol{x}_2, \cdots, \boldsymbol{x}_N\}$, with N observations and d variables (also referred to as dimensions), $f(\boldsymbol{X})$ denote the underlying functions of the GP, $\{f(\boldsymbol{x}_1), f(\boldsymbol{x}_2), \cdots, f(\boldsymbol{x}_N)\}$, and $\boldsymbol{y}$ be the output vector, which is actually observed, and can be corrupted by noise,

$$\boldsymbol{y} = f(\boldsymbol{X}) + \boldsymbol{\varepsilon} \tag{2}$$

where $\boldsymbol{\varepsilon}$ is a zero mean Gaussian noise process, with variance ${\sigma_N}^2$. Note that for the sake of conciseness, $f(\boldsymbol{X})$ will henceforth simply be denoted as $\boldsymbol{f}$.

In the Bayesian approach, the prior belief of the form of the GP, $\boldsymbol{f}$ is utilised along with the likelihood function of the observed data to calculate its posterior distribution. This can be expressed as,

$$\text{posterior} = \frac{\text{likelihood} \times \text{prior}}{\text{marginal likelihood}} \tag{3}$$

$$p(\boldsymbol{f}|\boldsymbol{y}, \boldsymbol{X}) = \frac{p(\boldsymbol{y}|\boldsymbol{X}, \boldsymbol{f})p(\boldsymbol{f}|\boldsymbol{X})}{p(\boldsymbol{y}|\boldsymbol{X})} = \frac{p(\boldsymbol{y}|\boldsymbol{X}, \boldsymbol{f})p(\boldsymbol{f}|\boldsymbol{X})}{\int p(\boldsymbol{y}|\boldsymbol{X}, \boldsymbol{f})p(\boldsymbol{f}|\boldsymbol{X})d\boldsymbol{f}} \tag{4}$$

where $p(\boldsymbol{f}|\boldsymbol{y}, \boldsymbol{X})$ is the posterior distribution (probability of functions given the outputs and inputs, $p(\boldsymbol{y}|\boldsymbol{X}, \boldsymbol{f})$ is the likelihood function (probability of outputs, given inputs and functions), $p(\boldsymbol{f}|\boldsymbol{X})$ is the prior distribution (probability of the functions, given inputs), and $p(\boldsymbol{y}|\boldsymbol{X})$ is the marginal distribution (probability of outputs, given only the inputs). $p(\boldsymbol{y}|\boldsymbol{X})$ is independent of the functions because it is integrated over the entire functional space of $\boldsymbol{f}$.

In the framework of GPs, functions between inputs and outputs can be completely defined by a mean function, $m(\boldsymbol{x})$, and a covariance function, $k(\boldsymbol{x}_p, \boldsymbol{x}_q)$, and these are in turn defined by hyperparameters [22]. Note that the subscripts are used to distinguish one input vector from another. This definition is analogous to a Gaussian distribution, which can be fully described using a mean and a variance. GPs therefore provide a distribution of functions between inputs and outputs. The mean and covariance functions are expressed as,

$$m(\boldsymbol{x}) = E[f(\boldsymbol{x})] \tag{5}$$

$$k(\boldsymbol{x}_p, \boldsymbol{x}_q) = E[(f(\boldsymbol{x}_p) - m(\boldsymbol{x}_p))(f(\boldsymbol{x}_q) - m(\boldsymbol{x}_q))] \tag{6}$$

The covariance function is a vital ingredient of the GP, as it characterises the general properties of the GP. Typically, when $\boldsymbol{x}_p$ and $\boldsymbol{x}_q$ are almost identical, $k(\boldsymbol{x}_p, \boldsymbol{x}_q)$ would yield high values (high correlation), and as they grow in distance, the values reduce in magnitude (low correlation). Due to this, when

predictions are performed, new inputs that geometrically lie close to previously observed inputs will have a greater influence than those that lie far away.

2.3.1. Covariance functions

The choice of covariance functions is one of fundamental importance. Depending on the problem being solved, there are numerous covariance functions (also referred to as kernels in the literature) available to use. Examples include squared-exponential, Matérn, γ-exponential, rational quadratic, and the Bayesian linear covariance functions [22]. These functions can be combined using basic algebra (addition, multiplication, etc.) to form advanced covariance functions. In the work presented in this article, only the squared-exponential and Bayesian linear covariance functions are used, and hence the discussion will be focussed on these.

The squared-exponential covariance function is defined as,

$$k_{SE}(\boldsymbol{x}_p, \boldsymbol{x}_q) = {\sigma_f}^2 \exp\left(-\frac{(\boldsymbol{x}_p - \boldsymbol{x}_q)^T(\boldsymbol{x}_p - \boldsymbol{x}_q)}{2\lambda^2} \right) \tag{7}$$

where ${\sigma_f}^2$ is a hyperparameter that represents the signal variance, and λ is a length-scale hyperparameter (which controls how smooth the function appears). Note that $(\boldsymbol{x}_p - \boldsymbol{x}_q)^T(\boldsymbol{x}_p - \boldsymbol{x}_q)$ is simply the squared Euclidean distance between input points.

The Bayesian linear covariance function is defined as,

$$k_{BL}(\boldsymbol{x}_p, \boldsymbol{x}_q) = {\sigma_0}^2 \boldsymbol{x}_p \cdot \boldsymbol{x}_q \tag{8}$$

where ${\sigma_0}^2$ is also a hyperparameter that represents the signal variance. This covariance function is classed as a *dot-product covariance function*, for obvious reasons.

Finally, input noise can also be taken into account, i.e. when observations are noisy. This is defined via,

$$k_N(\boldsymbol{x}_p, \boldsymbol{x}_q) = {\sigma_N}^2 \delta(\boldsymbol{x}_p, \boldsymbol{x}_q) = {\sigma_N}^2 \boldsymbol{I} \tag{9}$$

where ${\sigma_N}^2$ is a hyperparameter that represents the variance of the noise process and δ is the Kronecker-delta function, which can simply be viewed as the identity matrix, $\boldsymbol{I}$.

For the GPs associated with this work, a sum of the above covariance functions was considered to explain the observed data. There are three distinct covariance matrices associated with the predictive GPs:

1. $\boldsymbol{K_\theta(X, X)}$: Covariance matrix between training data only. For the sake of convenience, this will simply be denoted $\boldsymbol{K_\theta}$.

$$\boldsymbol{K_\theta} = k_{SE}(\boldsymbol{x}_p, \boldsymbol{x}_q) + k_{BL}(\boldsymbol{x}_p, \boldsymbol{x}_q) + k_N(\boldsymbol{x}_p, \boldsymbol{x}_q) \tag{10}$$

2. $\boldsymbol{K_*(X, X^*)}$: Cross covariance matrix between training and test data. The asterisk superscript denotes test data. Note that $\boldsymbol{K_*(X^*, X)}$ can also be calculated separately, but it is simply the transpose of $\boldsymbol{K_*(X, X^*)}$. For conciseness, $\boldsymbol{K_*(X, X^*)}$ will be denoted $\boldsymbol{K_*}$.

$$\boldsymbol{K_*} = k_{SE}(\boldsymbol{x}_p, \boldsymbol{x}_q^*) + k_{BL}(\boldsymbol{x}_p, \boldsymbol{x}_q^*) \tag{11}$$

3. $\boldsymbol{K_{**}(X^*, X^*)}$: Covariance matrix between test data only. This will simply be denoted $\boldsymbol{K_{**}}$.

$$\boldsymbol{K_{**}} = k_{SE}(\boldsymbol{x}_p^*, \boldsymbol{x}_q^*) + k_{BL}(\boldsymbol{x}_p^*, \boldsymbol{x}_q^*) \tag{12}$$

It should be noted that in the latter two covariance functions, the noise term is not added for the prediction of the noise-free underlying function, $\boldsymbol{f^*}$.

Now that the background of GPs has been introduced, it is necessary to discuss how they can be used in regression problems. Matters will be elaborated using the terms in the Bayes' theorem: the prior, the likelihood, and the marginal likelihood. The marginal likelihood is utilised in the training process, where the hyperparameters that define the GP are learnt.

2.3.2. The prior distribution

The prior to the functions, $\boldsymbol{f}$ has the form,

$$\boldsymbol{f} \sim \mathcal{GP}(0, \boldsymbol{K}) \tag{13}$$

where the 0 indicates a zero-mean function. $\boldsymbol{K}$ is now the covariance matrix, without the noise term. The benefit of incorporating a mean function is that in the absence of training data in a given region of the input space, the prediction of the GP will approach the mean trend that is defined by the mean function. This is because it specifies a belief in the relationship between inputs and outputs having a certain functional form. It is noteworthy that it is not necessary to limit the form of the GP using a mean. This is because, in practice, data is typically de-trended, and so, mean trends are already removed [23]. In any case, the prior distribution gets updated in each step of the training process, and so the mean function can be set to zero. However, this does not imply that the output of the GP will have zero mean, and is hence not a limiting issue. It has a distribution,

$$p(\boldsymbol{f}|\boldsymbol{X}) = \mathcal{N}(0, \boldsymbol{K}) \tag{14}$$

2.3.3. The likelihood distribution

$\boldsymbol{f}$ is a realisation of the underlying GP with inputs, $\boldsymbol{X}$. Because $\boldsymbol{y}$ is simply $\boldsymbol{f}$ with additive Gaussian noise ($\mathcal{N}(0, {\sigma_N}^2)$), the likelihood distribution can be stated as,

$$p(\boldsymbol{y}|\boldsymbol{X}, \boldsymbol{f}) = \mathcal{N}(\boldsymbol{f}, {\sigma_N}^2\boldsymbol{I}) \tag{15}$$

2.3.4. The marginal likelihood and hyperparameter learning

The denominator in equation (4) is important in estimating (or learning) the hyperparameters. It is also normally distributed with the form,

$$p(\boldsymbol{y}|\boldsymbol{X}) = \mathcal{N}(0, \boldsymbol{K_\theta}) \tag{16}$$

where $\boldsymbol{K_\theta}$ is the covariance matrix with additive noise, i.e. $\boldsymbol{K_\theta} = \boldsymbol{K} + {\sigma_N}^2\boldsymbol{I}$. The marginal likelihood is usually expressed in terms of its logarithmic transformation: the log marginal likelihood [22],

$$\mathcal{L} = \log p(\boldsymbol{y}|\boldsymbol{X}) = -\frac{1}{2}\boldsymbol{y}^T {\boldsymbol{K_\theta}}^{-1}\boldsymbol{y} - \frac{1}{2}\log|\boldsymbol{K_\theta}| - \frac{N}{2}\log(2\pi) \tag{17}$$

where N is the number of training points, and the other definitions are consistent with the preceding discussion. When the hyperparameters of the covariance functions are being learnt, the goal is to maximise the marginal likelihood with respect to the hyperparameters. Alternatively, the negative log marginal likelihood can also be minimised. If the hyperparameters of the covariance functions can be combined in a tuple, $\boldsymbol{\varphi} = \{\sigma_f, \lambda, \sigma_0, \sigma_N\}$, the partial derivative of the negative log marginal likelihood can be expressed as,

$$\frac{\partial}{\partial \boldsymbol{\varphi}_i}(-\mathcal{L}) = \frac{1}{2}tr\left[{\boldsymbol{K_\theta}}^{-1}\frac{\partial \boldsymbol{K_\theta}}{\partial \boldsymbol{\varphi}_i}\right] - \frac{1}{2}\boldsymbol{y}^T {\boldsymbol{K_\theta}}^{-1}\frac{\partial \boldsymbol{K_\theta}}{\partial \boldsymbol{\varphi}_i}{\boldsymbol{K_\theta}}^{-1}\boldsymbol{y} \tag{18}$$

where tr is the trace operator (i.e. sum of the diagonal elements of the matrix). In practice, the negative log marginal likelihood of GPs may have several local minima. Therefore, solving this problem becomes one of numerical optimisation. There are several routes one can take, for example gradient descent, differential evolution, Broyden-Fletcher-Goldfarb-Shanno algorithm, etc. There are no right or wrong choices in the optimisation routines, but each optimiser can have advantages and disadvantages associated with them. In this work, the Nelder-Mead simplex algorithm was used as the optimiser [24].

2.3.5. Posterior distribution

The posterior distribution can be obtained by combining equations (14), (15) and (16), and using Bayes' theorem - equation (3); this is given by,

$$p(\boldsymbol{f}|\boldsymbol{X}, \boldsymbol{y}) = \mathcal{N}(\boldsymbol{K}^T {\boldsymbol{K_\theta}}^{-1}\boldsymbol{y}, \boldsymbol{K} - \boldsymbol{K}^T {\boldsymbol{K_\theta}}^{-1}\boldsymbol{K}) \tag{19}$$

2.3.6. Predictions using GPs

Thus far, the necessary ingredients of the GPs have been shown. The next task is to use these for the main goal of the GPs: prediction. Let $\boldsymbol{x}^*$ denote a test input vector, (i.e. a matrix which is now going to be used to predict the outputs). The corresponding noise-free test output is $\boldsymbol{f}^*$. Now, the observed (noisy) training outputs and the noise-free test outputs are jointly Gaussian distributed according to the prior distribution, and can be expressed as,

$$\begin{bmatrix} \boldsymbol{y} \\ \boldsymbol{f}^* \end{bmatrix} = \mathcal{N}\left(0, \begin{bmatrix} \boldsymbol{K_\theta} & \boldsymbol{K_*} \\ \boldsymbol{K_*}^T & \boldsymbol{K_{**}} \end{bmatrix}\right) \tag{20}$$

where the respective covariance matrices were defined in equations (10), (11), and (12). The corresponding conditional distribution can be expressed as,

$$p(\boldsymbol{f}^*|\boldsymbol{X}, \boldsymbol{y}, \boldsymbol{x}^*) = \mathcal{N}(\bar{\boldsymbol{f}}^*, cov(\boldsymbol{f}^*)) \tag{21}$$

where the predictive mean, $\bar{\boldsymbol{f}}^*$ of the GP can be calculated using,

$$\bar{\boldsymbol{f}}^* = \boldsymbol{K_*}^T \boldsymbol{K_\theta}^{-1} \boldsymbol{y} \tag{22}$$

and the predictive covariance, $cov(\boldsymbol{f}^*)$ of the GP can be calculated using,

$$cov(\boldsymbol{f}^*) = \boldsymbol{K_{**}} - \boldsymbol{K_*}^T \boldsymbol{K_\theta}^{-1} \boldsymbol{K_*} \tag{23}$$

The diagonal of the matrix given by equation (23) is then used to give the uncertainties (in terms of variance) in prediction. The noise variance can be added to the predictive variance to take uncertainty related to noisy test outputs into consideration, and hence instead of finding the predictive distribution of $\boldsymbol{f}^*$, the predictive distribution of $\boldsymbol{y}^*$ can be calculated. Note that this does not affect the predictive mean, only the predictive covariance.

2.4. Application of machine learning

Figure 5 provides an overview of the flow of data in the machine learning phase of the SHM scheme, which includes training, optimisation, and Gaussian Process (GP) predictions.

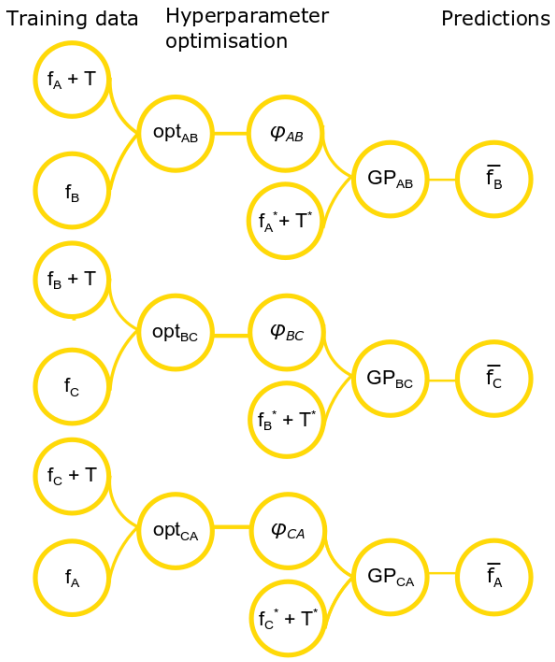

Figure 5: Flow of data in the proposed methodology.

Figure 5 shows that there are a total of three GPs that perform the predictions. However, before any predictions could be performed, the first task was to learn the hyperparameters, φ of the models that controlled their predictive capabilities - and this entailed a training process. Here, a subset of the selected feature data were selected for the training.

When choosing the training data, it was important to consider only data when the blades were in a normal (healthy) condition. However, the conditions of the blades were not known beforehand. It was therefore decided that training data would only be selected from the first two years of the turbine operation, assuming that the blades were in a normal condition throughout this period. Within this period of two years, 2500 data points were randomly selected from a uniform distribution. Choosing this two year time period for training ensured that the selected data spanned the entire normal operating range of the blades.

The random selection ensured that there was no bias to any specific operating condition in the training phase. It should be noted that more training data would increase the computational costs of the GPs, since computational costs are $\mathcal{O}(N^3)$, where N is the number of training points. There are sparse methods available to reduce the computational load associated with training, but these were not employed in this work.

The estimated frequencies, f of one blade (e.g. for blade A, f_A) were combined with the ambient temperatures, T to form a matrix of the training inputs. Referring to Section 2.3, this is the matrix, $\boldsymbol{X}$. The estimated frequencies of another blade (e.g. for blade B, f_B) formed the training outputs. Referring to Section 2.3, this is the vector, $\boldsymbol{y}$. These training data were used to learn the hyperparameters (φ) for the respective GPs via the Nelder-Mead method. During the learning phase, the covariance matrices, equations (10 - 12) were evaluated several times, which is why it was stated that the computational costs of GPs increases significantly with the number of training points. The hyperparameters selected corresponded to those that yielded the largest maximum log marginal likelihood, equation (17). The Nelder-Mead algorithm identifies this by minimising the negative log marginal likelihood, i.e. the negative of equation (17). These hyperparameters control the generalisation properties of the GPs, i.e. how the GPs adapt to the nature of the problem being tested. The asterisk symbols, * shown in Figure 5 are used to denote test data, i.e. data not included in the training set. The test data, f^* and T^* were combined in a matrix (referred to as the matrix, $\boldsymbol{X^*}$ in Section 2.3), and were then used in the various GPs (GP_{AB}, GP_{BC}, and GP_{CA}), using the respective hyperparameters (φ_{AB}, φ_{BC}, and φ_{CA}), to evaluate the predicted frequencies, $\bar{f_B}$, $\bar{f_C}$, and $\bar{f_A}$, respectively. The bar symbol ($^-$) indicates a prediction, rather than an actual estimate of the frequencies. The predictions are referred to as $\boldsymbol{f^*}$ in Section 2.3, and are calculated using equation (22). To elucidate,

- in GP_{AB}, ${f_A}^*$ and T^* were used to predict $\bar{f_B}$ using hyperparameters φ_{AB},

- in GP_{BC}, ${f_B}^*$ and T^* were used to predict $\bar{f_C}$ using hyperparameters φ_{BC}, and
- in GP_{CA}, ${f_C}^*$ and T^* were used to predict $\bar{f_A}$ using hyperparameters φ_{CA}.

2.5. Diagnostics and actions

Figure 6 shows the tasks involved in the diagnostics and actions section.

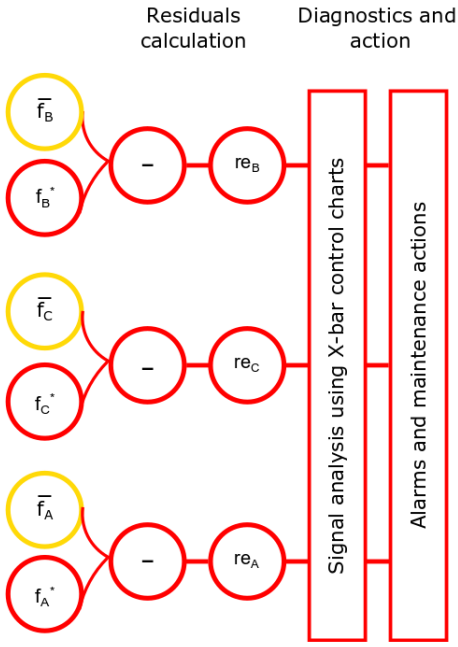

Figure 6: Diagnostics of GP residuals.

Following the frequency predictions for each blade via the respective GPs, residual errors were calculated between the predicted frequencies and the actual estimations (for example, the GP residual error for blade B, re_B was defined as the difference between $\bar{f_B}$ and ${f_B}^*$).

The assessment of whether the blades were healthy or not was performed using X-bar control charts. In the X-bar control charts, averages of the GP residuals were taken at regular time intervals. For the purposes of this work,

averages were taken regularly over a 28 day interval. During a brief period that followed the GP training phase detailed in the previous section, 3σ thresholds were also calculated. These were evaluated over a period of 6 months. The calculated averages of the X-bar control chart were then compared with the 3σ thresholds, and if the averages exceeded the thresholds, it was concluded that the blades were no longer in a normal condition.

During the development of this SHM system, maintenance actions were not taken. In practice, once the GP residuals surpass the thresholds of the X-bar control charts, warnings would be generated before alarms occur. In such a scenario, maintenance technicians would be sent to inspect the blades, they would assess the level of damage, and finally would decide whether to repair or replace the turbines.

2.6. Summary

The following summarises the SHM system as detailed in the preceding sections.

1. Data acquisition.
2. Data cleansing (removal of outliers).
3. Feature selection.
4. GP training (identification of hyperparameters).
5. GP prediction.
6. Calculation of residual errors.
7. X-bar control chart analysis of GP residuals.

3. Case studies

Now that the diagnostic methodology and theory have been described in detail, it is important to illustrate its performance. Prior to the results and discussion of the case studies, the detailed steps of the employed machine learning methodology are stated.

3.1. Detailed implementation

In this section, a detailed description is given/reiterated regarding the implementation of the machine learning methods described thus far, referring to the seven steps in Section 2.6. That is,

1. Data acquisition: In the following sections, three sets of data are introduced. The data are either synthesised or acquired directly from operational wind turbines. In the synthesised case, it is acknowledged that the data does not reflect the true behaviour of blades. However, the method of the data synthesis is described in detail to allow readers to reproduce them and apply the machine learning methodology. In the two cases where the data is acquired from operational wind turbines, a blade on each turbine shown was known to be damaged, and as a result, it either needed to be repaired or replaced. Damage can occur at various locations across the length of the blade, and the types of damage in blades are predominantly cracks or delaminations. In some cases, both occur at the same time. Due to confidentiality issues, however, the specific damage types and locations are not disclosed here.
2. Data cleansing (removal of outliers): In the case of the synthesised data, outliers are not included in the data, hence this process is not conducted. In the case of the real data, the standard deviations of the dataset are calculated, and data points outside 3σ of the data are iteratively removed. This process is repeated until the difference in standard deviation between subsequent iterations is less than 0.1. This value is empirically identified to ensure that outliers due to blade damage are not removed. Note that when an outlier is removed from one of the data channels, data from the other channels with the same timestamp (which may not necessarily be outliers) are also removed.
3. Feature selection: The main features of interest are the edge frequencies of the blades. It is shown in Example 3 below that the inclusion of temperature as a feature improves the performance of the GPs.

4. GP training (identification of hyperparameters): For each example shown, 2500 training points are selected from a period when the blades on the turbine are considered 'healthy'. In the case of data from the real turbines, this was chosen to be the first two years of turbine operation. The training points, indexed by the data point numbers, are sampled uniformly via that index. Standard normalisation, equation (1) is applied to the entire dataset using the mean and standard deviation values of the training data points. Next, the training input and output edge frequency data are prepared into three pairs (that is, f_A and f_B, f_B and f_C, and f_C and f_A; temperature, T is also included for the training inputs). The hyperparameters, ϕ_{AB}, ϕ_{BC}, and ϕ_{CA}, are then identified by minimising the negative log marginal likelihood, which is equivalent to maximising log marginal likelihood, equation (17). The Nelder-Mead algorithm is used to accomplish this.
5. GP prediction: The identified hyperparameters for each GP are used with the rest of the edge frequency and temperature data (${f_A}^*$, ${f_B}^*$, ${f_C}^*$, and T^*) are used to evaluate the predicted edge frequencies, $\bar{f_A}$, $\bar{f_B}$, and $\bar{f_C}$ using equation (22). Note that for relatively large datasets such as those used in this work, computer memory can easily be used up since the covariance matrices would be too large. For this reason, the GP predictions are performed in smaller chunks (1000 points at a time in this case).
6. Calculation of residual errors: The GP residuals are calculated by subtracting the actual edge frequency data from the predicted edge frequencies. That is,

$$\begin{aligned} re_A &= \bar{f_A} - {f_A}^* \\ re_B &= \bar{f_B} - {f_B}^* \\ re_C &= \bar{f_C} - {f_C}^* \end{aligned} \tag{24}$$

7. X-bar control chart analysis of GP residuals: In this step, the X-bar control charts of the residuals are calculated. This is performed by calculating averages of the residual errors over periods spanning 28 days. As the GPs

are trained over the first two year period on the examples shown from real wind turbines, it is important that the thresholds for the X-bar control chart analyses are not evaluated over the same period. This is because, generally, residual errors are low over training data since optimisation routines aim to minimise these errors as much as possible when identifying the hyperparameters. Thus, such practices can potentially lead to stringent thresholds that may increase false alarm rates. For this reason, a six-month period immediately after the initial two-year training period is chosen. As the standard deviation of the errors during this period may be occasionally large, the following technique is used to calculate robust thresholds. For each of the residual error datasets over this six-month period, small subsets are randomly selected several times (in this work, 20 times). For each subset i, the mean μ_i and standard deviation σ_i values are calculated. Finally, averages of the mean and standard deviation data are calculated, $\bar{\mu}$ and $\bar{\sigma}$, respectively. The thresholds, thr are then calculated using,

$$thr = \bar{\mu} \pm 3\bar{\sigma} \tag{25}$$

The residual errors for each blade are then compared to the upper and lower thresholds for each blade. Once the residual errors exceed these thresholds, the blade is assumed to be damaged.

3.2. Example 1: Synthesised data

In this example, a demonstration of the algorithm is described using some synthesised data. It must be noted that due to confidentiality agreements in effect, signals simulating the actual blade physics (and subsequent frequency estimations of the blades) cannot be reported. Instead, the edge frequency data of one blade is synthesised using a non-zero mean normal distribution. The edge frequency data of the second blade is set to be equal to that of the first blade with some additional noise. Finally, the third blade initially has the same edge

frequencies of the first blade, but 'deteriorates' over time by means of a negative linear gradient. That is,

$$f_A = \mathcal{N}(\mu_A, \sigma^2) \tag{26}$$

$$f_B = f_A + \mathcal{N}(0, \sigma^2) \tag{27}$$

$$f_C = f_A + d_C + \mathcal{N}(0, \sigma^2) \tag{28}$$

where d_C is a vector of zeros followed by a line with a negative gradient. That is,

$$d_C = \{\mathbf{0}, m\boldsymbol{x} + c\} \tag{29}$$

In this work, 360000 data points were generated. Only the first half of the data points of Blade C are considered 'healthy'. The length of the vector of zeros in equation (29) is therefore 180000. The rest of the vector d_C, which is indexed by the data point number, $\boldsymbol{x}$ (i.e. 180001 to 360000) has a gradient, m, of -1×10^{-7} and a y-intercept value, c of 0.018. Whilst not realistic, μ_A is set to 10 and σ^2 has a value of 0.01.

Figure 7 illustrates the synthesised edge frequencies of the three blades.

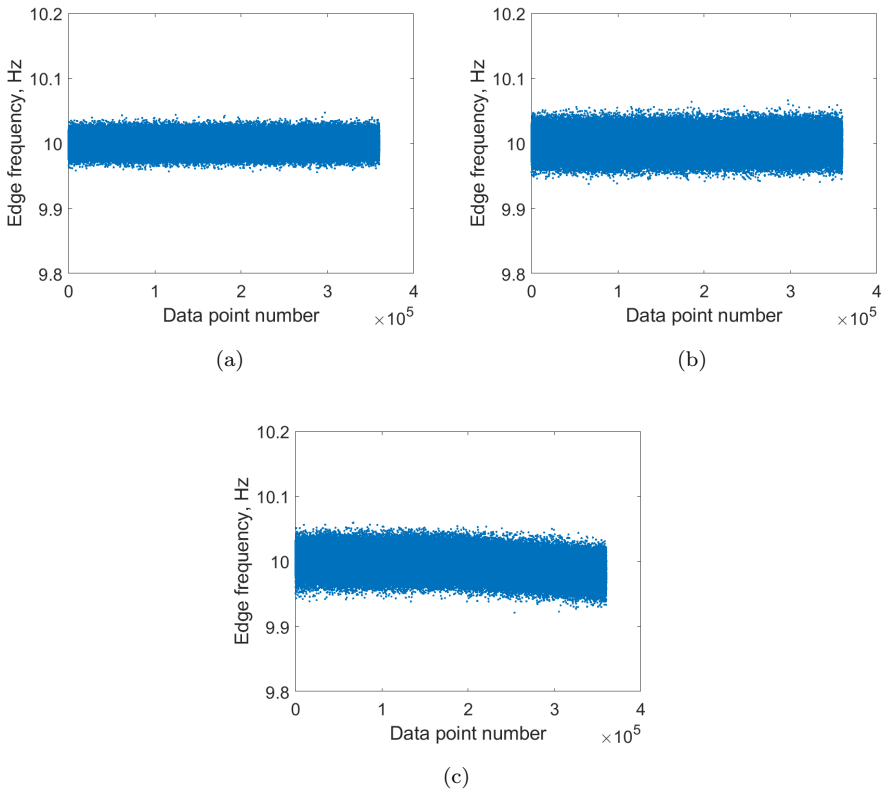

Figure 7: Synthesised edge frequency data for: (a) Blade A, (b) Blade B, and (c) Blade C

Referring to Section 2.6, the above description explains the data acquisition and feature selection processes. That is, the data acquired is As outliers do not exist on the synthesised data,t covers the first three

The methodology, as described in Section 2, is applied. Figure 8 illustrates the residual errors between the actual and predicted frequencies. Note that due to data normalisation (which is required for numerical stability, as discussed in Section 2), the residual errors are scaled. It is clear that the 'damage' is identified as the residual errors of blades A and C diverge on the midway point. The residuals of blade B do not diverge since they do not rely on data from the damaged blade C (actual or predicted). Note that in reality, the dynamics of healthy blades may also be affected by the presence of a damaged blade, and

hence it may not always be possible to conclude which blade contains damage.

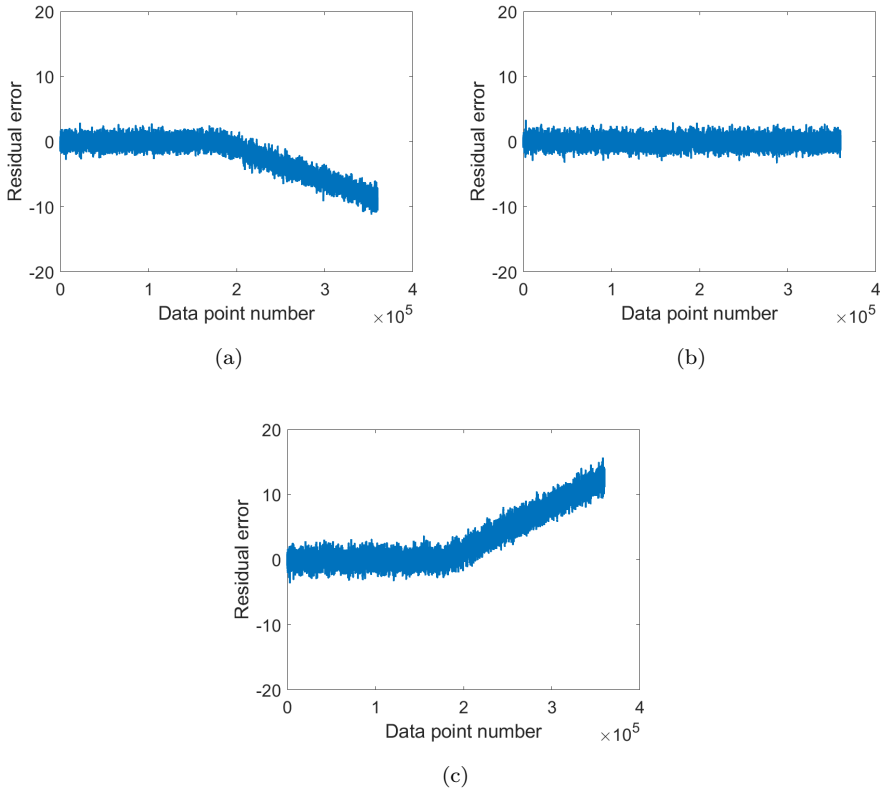

Figure 8: Residual errors between synthesised and predicted data for: (a) Blade A, (b) Blade B, and (c) Blade C

3.3. Example 2: Real turbine data

The correlation plots of this turbine were illustrated in Figures 2 and 3. In this example, one of the blades on the turbine was found to have some form of damage midway through Year 7 of turbine operation. Figure 9 illustrates the comparisons between the actual frequency estimations and the GP predictions for each blade. Note that on the following figures, the period between the vertical red lines illustrate the training period for the GPs, the period between the second vertical red line and the vertical green line illustrate the period the

3σ thresholds were calculated, and the vertical black lines indicate the date the damage was identified.

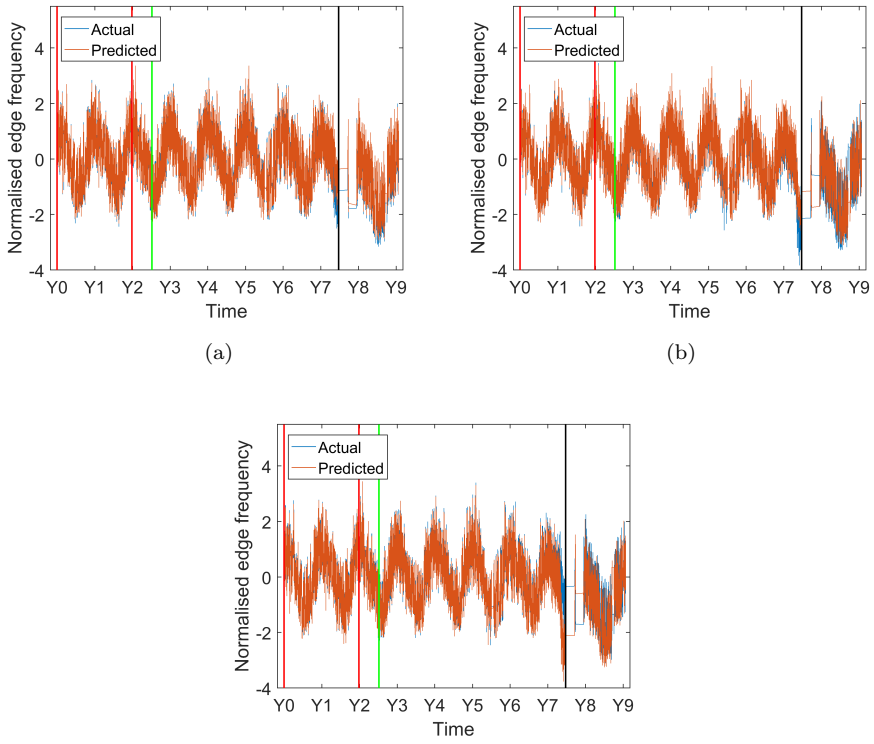

Figure 9: Comparison between actual estimated normalised edge frequencies and GP predictions for: (a) Blade A, (b) Blade B, and (c) Blade C in Site A.

Figures 10 (a) - (c) illustrate the residual errors corresponding to the results shown in Figures 9 (a) - (c), respectively.

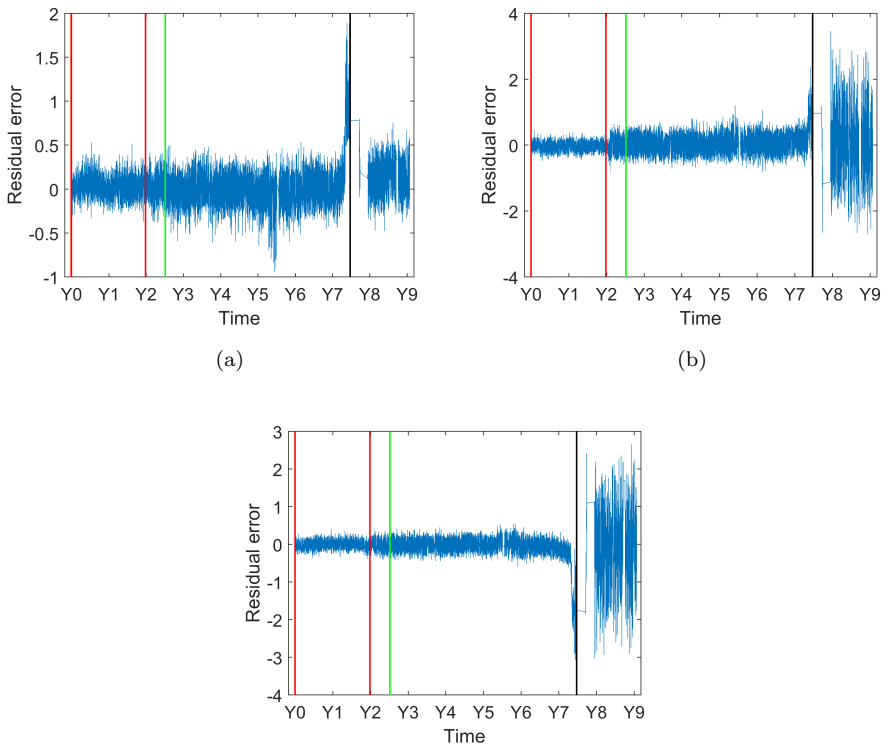

Figure 10: Residual errors between actual estimated normalised edge frequencies and GP predictions for: (a) Blade A, (b) Blade B, and (c) Blade C in Site A.

From Figures 9 and 10, it is clear that the GP predictions become less accurate as the date of damage approaches. As damage levels increase, and the properties of the blades change, the inputs to the GPs become geometrically further away than the inputs used during the training phase. Since machine learning methods in general, and GPs in particular, should not be used for extrapolation, the predictions become poorer, and hence, the residual errors grow. On closer inspection of Figure 10, it can be seen that just prior to the sharp increases in the GP residuals, there are small mean shifts that occur.

The corresponding X-bar control charts for Site A are shown in Figure 11. The averages were completed once every four weeks.

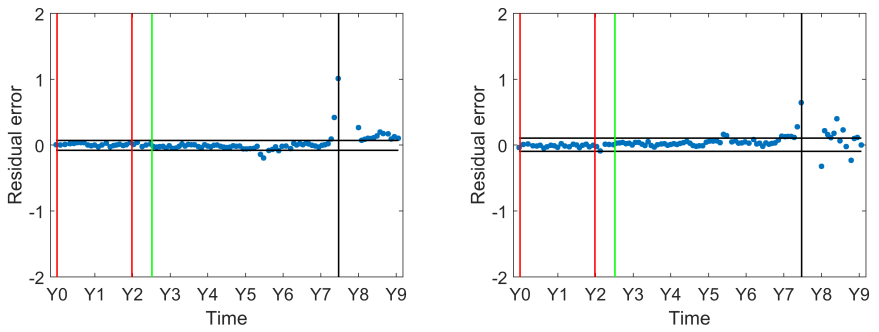

(a)

(b)

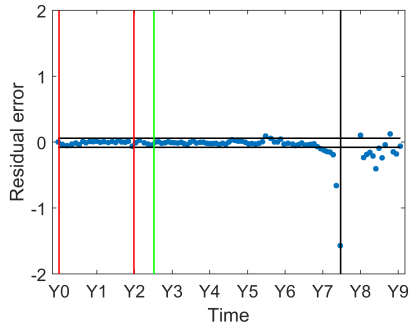

(c)

Figure 11: X-bar control charts of GP residuals for: (a) Blade A, (b) Blade B, and (c) Blade C in Site A.

The horizontal black lines indicate the calculated thresholds of the X-bar control charts. On analysing these charts in Figure 11, it can be seen that the GP residuals begin to indicate that the blade properties have changed roughly 6 months before the blade was remedied/replaced.

It is noteworthy that following the identification of damage, and the corresponding remedial action, there is a break down in the correlation between the pairs of blades. This is because the mechanical properties of the repaired/replaced blade are now different. Hence, whilst the residuals approach the original thresholds, they do not settle within them. This fact indicates that every time a remedial activity takes place, retraining is essential.

3.4. Example 3: Real turbine data

The correlation plots for this turbine are shown in Figure 12. Note that the temperature scales shown in these plots are normalised. In this example, all three correlation plots are noisy, although there is the expected positive correlation. The temperature effects are noticeable - at lower temperatures, when the blades are stiffer, the edge frequencies are higher, whereas at higher temperatures, the opposite is true.

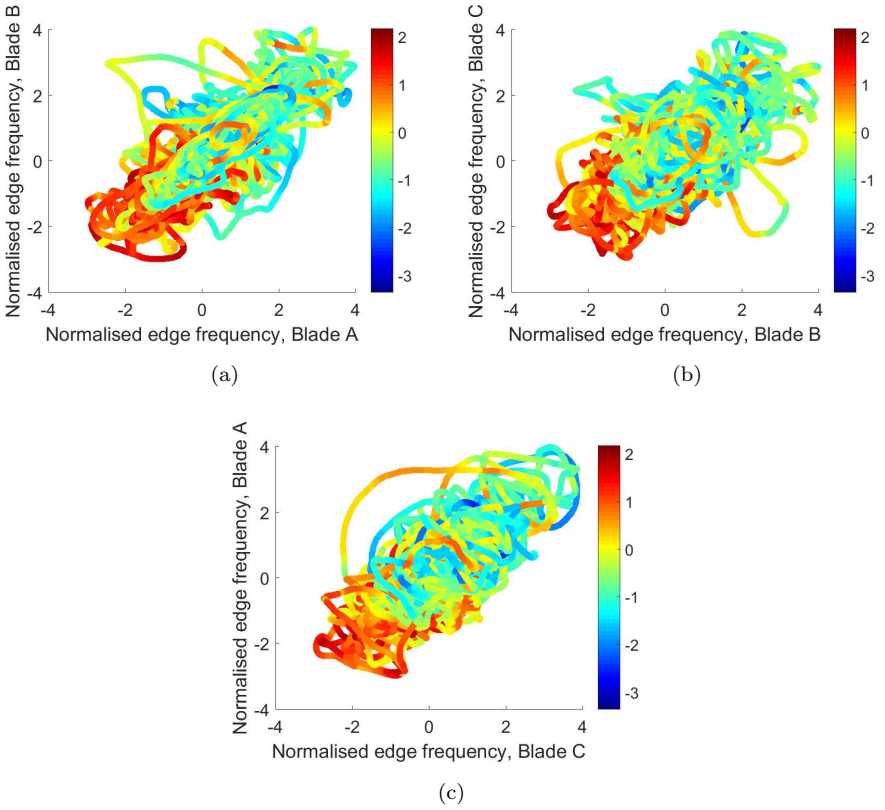

Figure 12: Correlation between normalised edge frequencies for: (a) Blade A vs. Blade B, (b) Blade B vs. Blade C, and (c) Blade C vs. Blade A in Site B.

Figure 12 illustrates how the GP predictions vary with the input edge frequencies and temperature. It is interesting to note how the GPs have identified a hidden structure within the noisy data - there are various bands of predictions

across the range of temperatures. These bands are both linear (captured by the linear kernel) and nonlinear (captured by the squared-exponential kernel).

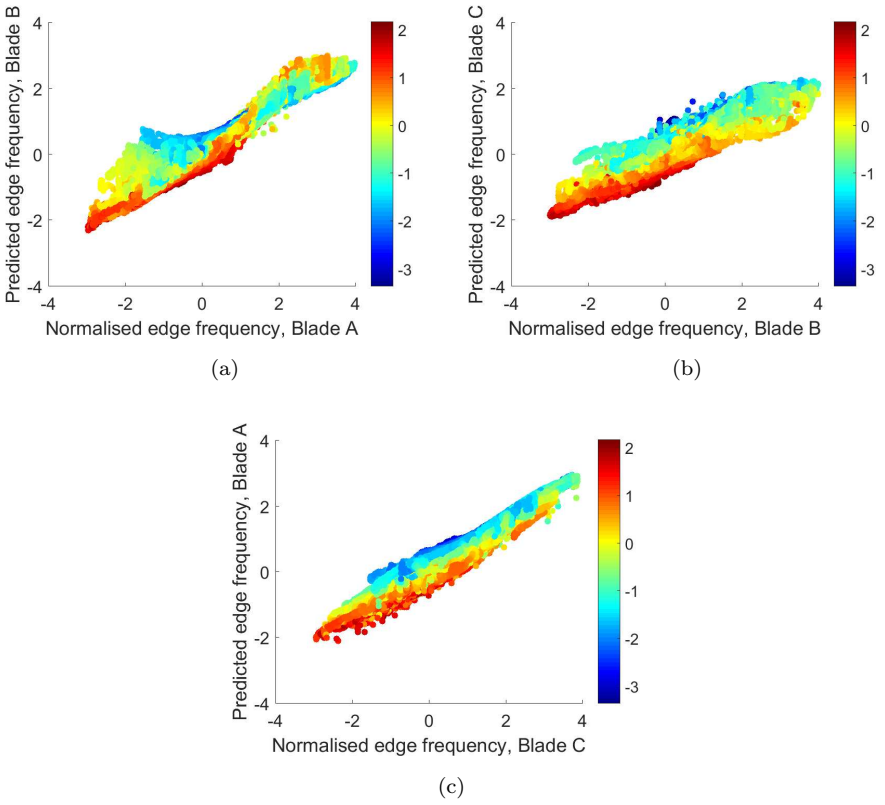

Figure 13: Correlation between normalised edge frequencies for: (a) Blade A vs. Blade B, (b) Blade B vs. Blade C, and (c) Blade C vs. Blade A in Site B.

Figures 14 and 15 compare the estimated and predicted edge frequencies. Once again, the seasonal variations are captured well. However, the amplitudes of the residual errors are high compared to those seen in Example 2, which is expected given the noisy estimates and correlations. The residuals in Figure 15 (a) and (b) indicate that an event occurred that changed the structural properties, and correlations between the blades around Year 4 as shown by the change in structure of the residuals. As the damage event approaches, there is a monotonic change in the residuals in Figure 15.

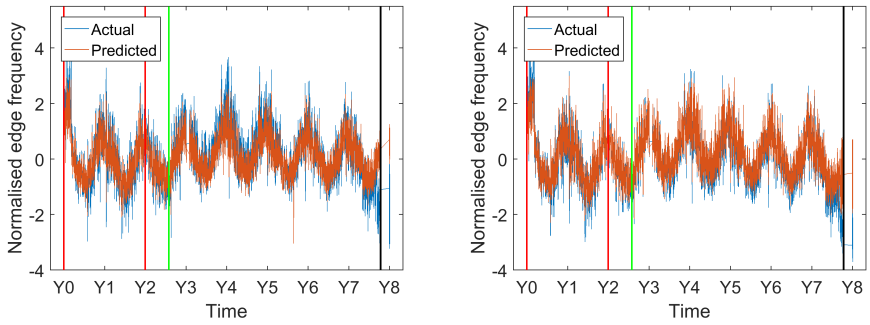

(a)

(b)

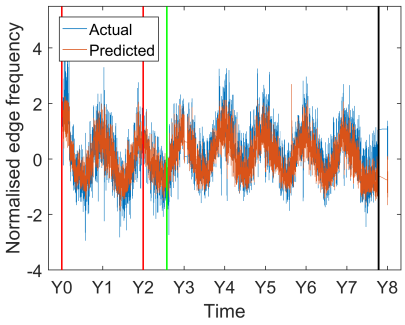

(c)

Figure 14: Comparison between actual estimated normalised edge frequencies, and GP predictions for: (a) Blade A, (b) Blade B, and (c) Blade C in Site B.

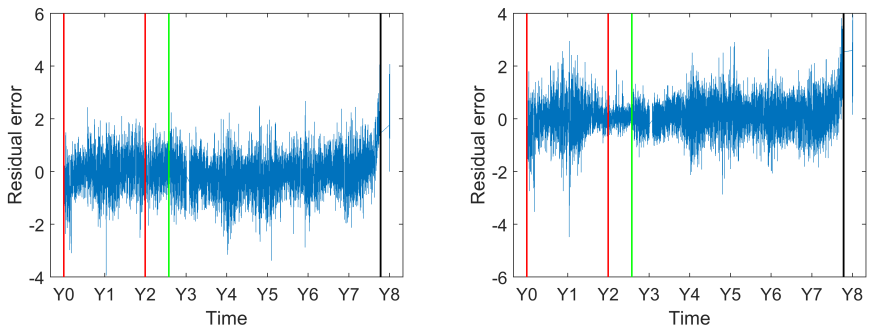

(a)

(b)

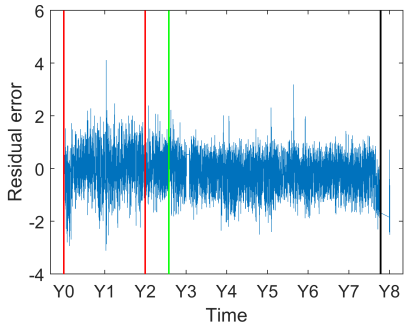

(c)

Figure 15: Residual errors between actual estimated normalised edge frequencies, and GP predictions for: (a) Blade A, (b) Blade B, and (c) Blade C in Site B.

Figure 16 shows the results from this final case study. Once again, the 3σ thresholds were exceeded in advance, this time only 3 months before the remedial activities to fix the blade took place. Furthermore, the amplitude of the threshold exceedance is not as pronounced as that seen in Example 2. This is primarily attributed to the noisy features used.

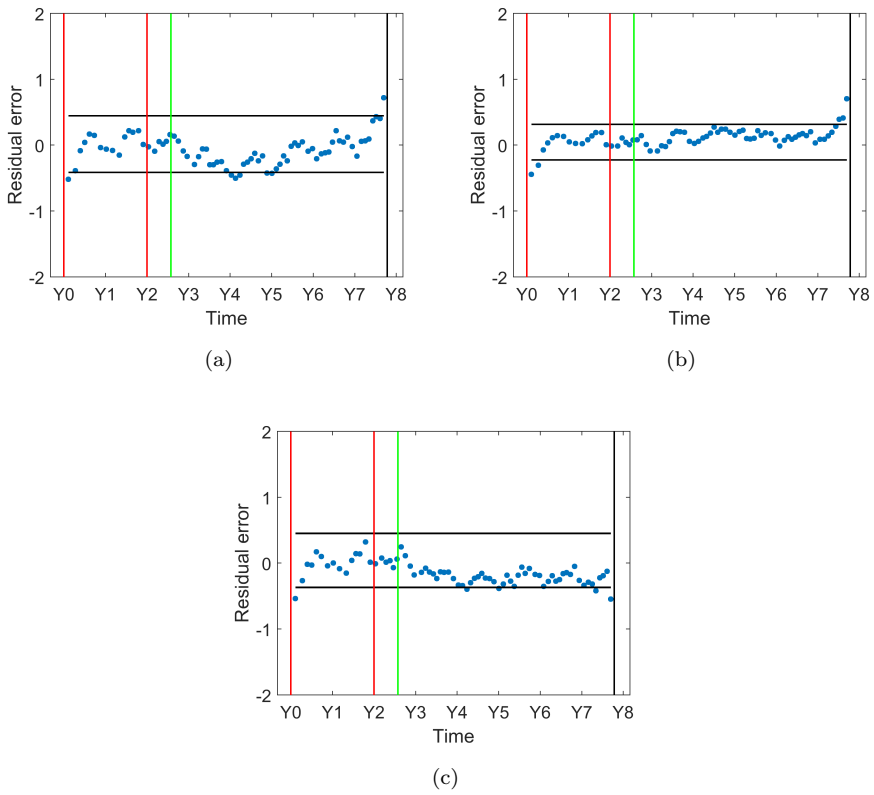

Figure 16: X-bar control charts of GP residuals for: (a) Blade A, (b) Blade B, and (c) Blade C in Site B.

4. Conclusions

In this article, a new diagnostic methodology for operational wind turbine blades has been proposed. Gaussian Processes (GPs) are used to predict the edge frequencies of one blade, given the edge frequencies of another blade and the ambient temperature. This may be viewed as another way of applying the Johansen procedure to cointegrate variables, as shown in [25]. The premise is that as long as no damage has taken place on the blade, the relationship between the edge frequencies of the respective blades should remain consistent. However, when damage does take place, the predictive capabilities of the GPs

would be affected, and the predictions would not be accurate. Hence, when damage takes place, the GP residuals (the difference between the actual and predicted edge frequencies) would grow in amplitude, and would hence act as informative damage indicators. X-bar control charts, along with 3σ thresholds, were used to indicate whether the blades were healthy or not.

A case study using synthesised data was used to illustrate the algorithm. Two other case studies from real turbines, where one of the blades was reported to sustain damage, were also shown to illustrate the diagnostic capabilities of the methodology proposed in this article. The results showed the successful implementation of this method whereby the respective damages were detected in advance of critical failure.

The key outcomes of this work are:

- Although the individual edge frequency time series of the blades are non-stationary, there exists a common and explicable trend between them, which can be learned.

- Due to the noisy estimation of the edge frequencies, there may not be a one-to-one mapping between the edge-frequency estimates of the pairs of blades. However, as long as the nominal trend of this correlation is captured by the GPs, the residual errors give sufficient information regarding the onset of damage as long as these frequencies being monitored are sensitive to the damage type and location.

- The addition of ambient temperature as a feature helps in the predictive capabilities of the GPs, especially when the edge-frequency estimates are noisy.

- The methodology of identifying correlations between two (or more) blades may be applied to different types of signals (for example, strains and displacements), although such signals may require additional pre-processing and other complementary features.

Acknowledgements

The authors would like to thank Siemens Gamesa Renewable Energy for funding this research; without their input, this project would not have been possible. The authors would also like to acknowledge the support of the following EPSRC grants: EP/R004900/1, EP/S001565/1, and EP/R003645/1.

References

[1] F. P. G. Márquez, A. M. Tobias, J. M. P. Pérez, M. Papaelias, Condition monitoring of wind turbines: Techniques and methods, *Renewable Energy* 46 (2012) 169–178.

[2] D. Li, S.-C. M. Ho, G. Song, L. Ren, H. Li, A review of damage detection methods for wind turbine blades, *Smart Materials and Structures* 24 (3) (2015) 033001.

[3] C. C. Ciang, J.-R. Lee, H.-J. Bang, Structural health monitoring for a wind turbine system: a review of damage detection methods, *Measurement Science and Technology* 19 (12) (2008) 122001.

[4] B. Yang, D. Sun, Testing, inspecting and monitoring technologies for wind turbine blades: A survey, *Renewable and Sustainable Energy Reviews* 22 (2013) 515–526.

[5] R. Raišutis, E. Jasiūnienė, R. Šliteris, A. Vladišauskas, The review of non-destructive testing techniques suitable for inspection of the wind turbine blades, *Ultragarsas* 63 (2) (2008) 26–30.

[6] J. Kaldellis, M. Kapsali, Shifting towards offshore wind energy - Recent activity and future development, *Energy Policy* 53 (2013) 136–148.

[7] C. Röckmann, S. Lagerveld, J. Stavenuiter, Operation and maintenance costs of offshore wind farms and potential multi-use platforms in the dutch north sea, *Aquaculture Perspective of Multi-Use Sites in the Open Ocean* (2017) 97–113.

[8] M. A. Rumsey, J. A. Paquette, Structural health monitoring of wind turbine blades, in: *Smart Sensor Phenomena, Technology, Networks, and Systems 2008*, Vol. 6933, International Society for Optics and Photonics, 2008.

[9] J. Sierra-Pérez, M. A. Torres-Arredondo, A. Güemes, Damage and nonlinearities detection in wind turbine blades based on strain field pattern recognition. FBGs, OBR and strain gauges comparison, *Composite Structures* 135 (2016) 156–166.

[10] A. Ghoshal, M. J. Sundaresan, M. J. Schulz, P. F. Pai, Structural health monitoring techniques for wind turbine blades, *Journal of Wind Engineering and Industrial Aerodynamics* 85 (3) (2000) 309–324.

[11] D. Adams, J. White, M. Rumsey, C. Farrar, Structural health monitoring of wind turbines: method and application to a HAWT, *Wind Energy* 14 (4) (2011) 603–623.

[12] J.-R. Lee, H.-J. Shin, C. C. Chia, D. Dhital, D.-J. Yoon, Y.-H. Huh, Long distance laser ultrasonic propagation imaging system for damage visualization, *Optics and Lasers in Engineering* 49 (12) (2011) 1361–1371.

[13] J. Tang, S. Soua, C. Mares, T.-H. Gan, An experimental study of acoustic emission methodology for in service condition monitoring of wind turbine blades, *Renewable Energy* 99 (2016) 170–179.

[14] N. Dervilis, M. Choi, S. Taylor, R. Barthorpe, G. Park, C. Farrar, K. Worden, On damage diagnosis for a wind turbine blade using pattern recognition, *Journal of Sound and Vibration* 333 (6) (2014) 1833–1850.

[15] S. G. Taylor, K. Farinholt, M. Choi, H. Jeong, J. Jang, G. Park, J.-R. Lee, M. D. Todd, Incipient crack detection in a composite wind turbine rotor blade, *Journal of Intelligent Material Systems and Structures* 25 (5) (2014) 613–620.

[16] C. Galleguillos, A. Zorrilla, A. Jimenez, L. Diaz, A. Montiano, M. Barroso, A. Viguria, F. Lasagni, Thermographic non-destructive inspection of

wind turbine blades using unmanned aerial systems, *Plastics, Rubber and Composites* 44 (3) (2015) 98–103.

[17] C. Niezrecki, P. Avitabile, J. Chen, J. Sherwood, T. Lundstrom, B. LeBlanc, S. Hughes, M. Desmond, A. Beattie, M. Rumsey, et al., Inspection and monitoring of wind turbine blade-embedded wave defects during fatigue testing, *Structural Health Monitoring* 13 (6) (2014) 629–643.

[18] M. Rumsey, J. Paquette, J. White, R. Werlink, A. Beattie, C. Pitchford, J. van Dam, Experimental results of structural health monitoring of wind turbine blades, in: *46th AIAA Aerospace Sciences Meeting and Exhibit*, 2008.

[19] J. Paquette, J. van Dam, S. Hughes, J. Johnson, Fatigue testing of 9 m carbon fiber wind turbine research blades, in: *46th AIAA Aerospace Sciences Meeting and Exhibit*, 2008.

[20] W. Yang, Z. Lang, W. Tian, Condition monitoring and damage location of wind turbine blades by frequency response transmissibility analysis, *IEEE Transactions on Industrial Electronics* 62 (10) (2015) 6558–6564.

[21] K.-S. Wang, V. S. Sharma, Z.-Y. Zhang, SCADA data based condition monitoring of wind turbines, *Advances in Manufacturing* 2 (1) (2014) 61–69.

[22] C. E. Rasmussen, C. K. I. Williams, *Gaussian Processes in Machine Learning*, The MIT Press, 2006.

[23] K. P. Murphy, *Machine Learning: A Probabilistic Perspective*, MIT Press, 2012.

[24] J. A. Nelder, R. Mead, A simplex method for function minimization, *The computer journal* 7 (4) (1965) 308–313.

[25] E. J. Cross, K. Worden, Q. Chen, Cointegration: a novel approach for the removal of environmental trends in structural health monitoring data, in:

Proceedings of the Royal Society of London A: Mathematical, Physical and Engineering Sciences, The Royal Society, 2011.